ELSEVIER

Contents lists available at ScienceDirect

Applied Ocean Research

journal homepage: www.elsevier.com/locate/apor



Field observations and long short-term memory modeling of spectral wave evolution at living shorelines in Chesapeake Bay, USA

Nan Wang ^a, Qin Chen ^{b,*}, Hongqing Wang ^c, William D. Capurso ^d, Lukasz M. Niemoczynski ^e, Ling Zhu ^a, Gregg A. Snedden ^c

- a Department of Civil and Environmental Engineering, Northeastern University, 400 SN, 360 Huntington Avenue, Boston, MA 02115, USA
- b Department of Civil and Environmental Engineering, and Department of Marine and Environmental Sciences, Northeastern University, 471 SN, Boston, MA 02115, USA
- U.S. Geological Survey, Wetland and Aquatic Research Center, Baton Rouge, LA 70808, USA
- ^d U.S. Geological Survey, New York Water Science Center, Coram, NY 11727, USA
- e U.S. Geological Survey, New Jersey Water Science Center, Lawrenceville, NJ 08648, USA

ARTICLE INFO

Keywords: Living shoreline Long short-term memory method Spectral wave modeling Wave forecast Marsh edge erosion

ABSTRACT

Living shorelines as a nature-based solution for climate change adaptation were constructed in many places around the world. The success of this type of projects requires long-term monitoring for adaptive management. The paper presents a novel framework leveraging scientific machine learning methods for accurate and rapid prediction of long-term hydrodynamic forcing impacting living shorelines using short-term measurements of water levels and wind waves in the largest estuary in the U.S. Different from existing data-driven wave prediction models focusing on significant wave heights, this study is focused on the prediction of wave energy spectra in shallow water using winds and tides as the input feature and short-term measurements of wave spectra and water depths as the label. Long Short-Term Memory (LSTM) models were developed using four-month wave measurements in the stormy seasons to predict integral wave parameters and energy spectra for multiple years. The developed models accurately predicted wave heights, peak periods, and energy spectra around the living shorelines, capturing complex wave dynamics, such as wave generation by wind, nonlinear wave-wave interactions, and depth-limited wave breaking in the shallow water of a large estuary. The validated models were then used to determine the long-term wave forcing impacting the living shorelines based on the modeled wave characteristics and spectra. Model results show that the surrogate models utilizing LSTM to predict wave spectra in the frequency domain enable long-term predictions of spectral wave evolution with a minimal computational cost. Our findings provide valuable insights into the efficacy of living shorelines in attenuating wave energy and demonstrate the utility of this approach in assessing the effectiveness of such living shoreline structures.

1. Introduction

Chesapeake Bay, situated on the East Coast of the United States, is renowned as the largest estuary in the country, spanning over 320 km from the Susquehanna River in Maryland to the Atlantic Ocean (Basco, 2020). It is an important ecological, economic, and recreational resource, providing habitat for many species of plants and animals, supporting commercial and recreational fishing, and attracting millions of visitors each year. However, the coastlines of Chesapeake Bay have been enduring chronic erosion, with estimated rates varying from 0 to 3 m/yr, primarily due to factors such as sea level rise, climate change, hurricanes, and storm surges (Sanford and Gao, 2018). Because of the

anticipated increase in global sea levels, the Chesapeake Bay shorelines and salt marshes will be at greater risk of damage. Consequently, the development of adaptation strategies becomes imperative in order to mitigate coastal erosion and address flood hazards stemming from extreme storms and climate change.

Traditionally, physical barriers like bulkheads, seawalls, revetments, groins, and breakwaters have been used to protect civil infrastructure from flooding and shorelines from erosion. However, these hard structures tend to increase wave reflection and cause scouring at the edges, leading to a loss of habitat, such as intertidal flats (e.g., O'Donnell, 2017). In recent years, more nature-based approaches (green approaches) have been incorporated into shoreline protection and

E-mail address: q.chen@northeastern.edu (Q. Chen).

^{*} Corresponding author.

restoration, such as using artificial oyster reefs (e.g., oyster castles, oyster shells) and vegetation (e.g., salt marshes, seagrass). One promising strategy is the adoption of a hybrid approach called "living shorelines," which combines both structural and natural elements. Living shorelines have the potential to mitigate coastal erosion and flood hazards by dissipating waves while providing crucial habitats. With the implementation of numerous living shoreline restoration projects along the Gulf Coast and Mid-Atlantic coast in the U.S., it becomes imperative to advance our comprehension of the efficacy of living shoreline structures to help inform upcoming restoration initiatives.

The correlation between wetland shoreline erosion rates and wave power has been established in previous studies (e.g., Schwimmer, 2001; Marani et al., 2011; McLoughlin et al., 2015; Leonardi et al., 2016; Zhu et al., 2020). Therefore, it is crucial to investigate the variations of wave power along the living shorelines. While integral wave parameters such as significant wave height and peak wave period are commonly utilized to characterize sea states and trends, they may not accurately represent the wave power within a complex wave field in shallow water. In the case of an estuary with living shorelines, relying solely on integral wave parameters to compute wave power could lead to underestimations (Zhu et al., 2020). Moreover, integral wave parameters can obscure essential characteristics of a wave field, potentially causing misinterpretation when confronted with complex wave conditions involving multiple wave systems propagating through a specific area (Wang et al., 2023b). In contrast, wave spectra offer a better approach to characterizing the wave field, providing precise insights into wave evolution with distinct energy sources and sinks. For instance, submerged vegetation can effectively dissipate the energy of the higher frequency band in a random wave field compared to the energy of the lower frequency band (Zhu and Chen, 2017). Therefore, obtaining accurate information about the wave spectra is essential as it enhances our understanding of the state of surface waves in coastal and estuarine regions, along with their long-term impacts on natural shorelines and civil infrastructure.

Despite the availability of conventional methods, such as processbased numerical simulations and field measurements, to obtain wave spectra of a study site, their applicability is often limited due to high computational and/or operational costs. For example, field measurements often require a substantial amount of time and financial resources, leading to data that is sparse in both spatial and temporal coverage. To address these challenges, researchers have turned to physics-based wave models such as SWAN (Booij et al., 1999) and WAVEWATCH (Tolman and Others, 2009) to simulate the evolution of wave spectra. However, applying these numerical models to simulate wave spectra in a living shoreline project area may require nested computational domains with varying spatial resolutions and the coupling of wave and nearshore-circulation models. These requirements can be expensive or impractical for long-term assessments over years and decades. Furthermore, certain numerical approximations, such as quadruplet wave-wave interactions and triad wave-wave interactions, can result in inaccurate predictions. For instance, Filipot and Cheung (2012) discovered that the original version of SWAN could not adequately capture the sub-harmonic component due to a lack of appropriate parameterization for describing nonlinear energy transfer towards the infra-gravity band. However, infra-gravity waves play a vital role in nearshore processes and require specific consideration in spectral wave modeling (Rijnsdorp et al., 2021). As an alternative approach, machine learning (ML) technology has emerged as a powerful tool that has revolutionized numerous scientific disciplines and introduced a novel paradigm to address current research needs (Xu et al., 2023). Scientific ML models can serve as substitutes for simulating wave spectra, eliminating the need for extensive computational resources. Additionally, these models can effectively handle the complexities of strong nonlinearity and high dimensionality.

In recent years, the utilization of ML in coastal and ocean engineering has gained significant attention. This interest is primarily driven by the accessibility of ML algorithms and the accumulation of

comprehensive datasets from numerical simulations, field measurements, and laboratory experiments (Xu et al., 2023). ML refers to a computational system capable of learning and improving from experience, typically in the form of datasets, without the need for explicit programming. Artificial Neural Network (ANN) has found extensive usage in coastal and ocean engineering applications to investigate nonlinear connections between input features and labels (e.g., Zheng et al., 2020; Bento et al., 2021; Mares-Nasarre et al., 2021; Elbisy and Elbisy, 2021). However, ANN models are limited in their ability to retain and utilize information from previous time steps. In contrast, Long Short-Term Memory (LSTM) models have the capacity to store information over longer time periods. LSTM models employ a memory cell to capture and retain past inputs and outputs, making them well-suited for handling time series data. They are particularly advantageous for tasks involving the identification of long-term dependencies in sequential data. Recent studies (Ni and Ma, 2020; Miky et al., 2021; Gao et al., 2021; Meng et al., 2021; Wei, 2021, 2022; Yao and Wu, 2022; Hao et al., 2022; Luo et al., 2022; Zhao et al., 2023; Sareen et al., 2023) have demonstrated the successful use of LSTM models for wave height forecasting. For instance, Jörges et al. (2021) developed an LSTM model to reconstruct and predict the nearshore wave field, demonstrating remarkable accuracy in predicting significant wave height for both long-term and short-term periods. Similarly, Ti et al. (2022) applied LSTM models to forecast spatial-temporal significant wave height in the West Pacific, demonstrating better accuracy and computational efficiency compared to physics-based numerical models. Furthermore, Zhang et al. (2023) introduced a memory curve into the conventional Support Vector Regression model, which significantly improved the accuracy of significant wave height prediction. However, the majority of existing ML models for wave prediction have primarily focused on wave height. There has been a lack of research dedicated to exploring the spatial-temporal evolution of wave spectra in shallow waters using ML methods.

This paper has two main objectives: (1) to examine the variations of energy spectra over time and space at the Fog Point living shoreline in Martin National Wildlife Refuge, Maryland, and (2) to develop LSTM models that can predict wave spectra and parameters at this specific site. The models were trained using wind, water level, and wave measurement data collected from February to May 2020. Subsequently, the trained models were employed to estimate wave parameters and energy spectra in 2020, 2021, and 2022, requiring minimal computational resources. This paper introduces an innovative approach for predicting energy spectra in the frequency domain in a large estuary, which can be extended to other living shoreline restoration projects to assess longterm variations in wave power, water level, and shoreline stability. We have applied a series of soft computing-based algorithms to address long-term wave prediction problems in coastal engineering. In our previous work (Wang et al., 2022b), we proposed a hybrid method that integrates a physics-based model (SWAN) with ML algorithms (i.e., bagged regression tree and ANN) to predict wave parameters and detect sources of error within the SWAN model. This hybrid approach can effectively overcome the limitation of using scarce observations to develop a predictive ANN model. To assess the long-term impact of constructed oyster reefs on wave fields in upper Delaware Bay, Wang et al. (2022c) developed ANN models to predict integral wave parameters, including significant wave height and peak wave period, based on short-term wave measurements. Since wave spectra can provide a better approach to characterizing complex wave fields, Wang et al. (2023b) focused on predicting wave energy density spectra as well as wave parameters using ANN models at the Chesapeake Bay Bridge-Tunnel with publicly available buoy data. Their goal was to separate the ocean swell spectra from the bay wave spectra at the estuarine entrance. In the current study, utilizing the capacity of LSTM algorithms to store and control relevant information over longer time periods, we developed a new data-driven model to investigate wave spectra along the headland-bay shoreline based on our field observations. Compared to

the estuarine entrance, the triad wave interactions are more pronounced at this study site due to nonlinear effects in the shallow water, affecting the spectral shape. Furthermore, modeling the impact of breakwaters on spectral wave evolution is challenging. This study tackled those issues.

The paper is structured as follows: In Section 2, detailed information is provided regarding the field experiment conducted and the LSTM model development, containing details about the model's input, output, and configuration. In Section 3, an evaluation is carried out to assess the effectiveness of the LSTM models in predicting wave parameters and energy spectra through a comparison of model outputs against field observations. Section 4 explores the application of transfer learning techniques to improve the accuracy of simulating high harmonics in shallow water due to triad wave-wave interactions. Furthermore, Section 4 also includes a representativeness test of the training data, ensuring the reliability of the year-long hindcast of wave energy spectra and wave power. In conclusion, Section 5 summarizes the main findings of the paper.

2. Methodology

2.1. Study site and field observations

Our study site (around 38° 1'47.64" N, 76° 2'34.08" W) is at the Fog Point shorelines in the Martin National Wildlife Refuge, Maryland, US located in the middle of the Chesapeake Bay (Fig. 1). The shorelines are exposed to prevailing winds, making them highly vulnerable to storms. Research shows that the shorelines along the northern and western shores of the refuge have receded at a rate of 0.61 to 5.5 m/yr from 2001 to 2013, leading to a loss of nearly 3.3 acres of prime fish and wildlife habitat annually (Perini Management Services, 2014). Therefore, it is important to address the issue of shoreline erosion. Rock breakwaters, sand nourishment, and planting of salt marsh species as living shoreline

structures were constructed along the Fog Point shoreline in the Martin National Wildlife Refuge in 2016 in response to Hurricane Sandy (2012) and future storms. The type of living shoreline is featured with the "headland(breakwater)-embayment-headland (breakwater)" pattern (Hardaway and Gunn, 2010). Rock breakwaters at the study site are typically 76.2 m long, with sand added behind connecting to the island. The tidal range is about 0.56 m, based on the measurements from a nearby NOAA station (8571421). The wave height variations at the study site were influenced by the combination of the structures and changes in bathymetry.

To evaluate the effectiveness of the living shoreline structures, six pressure transducers (i.e., wave gages (WG)) were deployed at low tides during February 10–14, 2020, and were originally planned to be retrieved in May 2020. Unfortunately, due to the COVID-19 travel restrictions, the retrieval was delayed until August 25, 2021, and only three of the gages (WG3, WG4, and WG5, Fig. 1(b)) were found. Furthermore, it was found that the wave data collected at WG5 after May 11 were inaccurate, possibly due to the gage being disturbed by an unknown force. As our study site is far away from the mouth of the Chesapeake Bay, the measured wave energy from the three gages was considered entirely generated locally by winds. As $T_{\rm p}$ from OCEANLYZ v2.0 may be incorrectly calculated when $H_{\rm m0}$ is very small, waves with $H_{\rm m0} < 1$ cm were excluded from further analysis. Field data are available in Wang et al. (2023a).

2.2. Machine learning models

To forecast wave parameters and spectra over an extended period, we constructed three composite LSTM networks at each gage location. These networks were developed by leveraging the domain knowledge regarding wave responses to forcing functions and the interrelation among wave parameters. To ensure the accuracy of the modeled long-



Fig. 1. (a) A map displaying the locations of the wave gages and the structure. (b) Salt marsh plants, S. alterniflora grow behind the breakwaters. The photograph was taken on July 11, 2017, nearly one year after breakwater construction (Photograph taken by Hongqing Wang, U.S. Geological Survey). (c) An illustration displaying the study area, indicated by a yellow triangle representing Fog Point Beach, along with nearby NOAA wind stations denoted by red dots in Chesapeake Bay. The small map shows Chesapeake Bay marked by a red dot.

term wave parameters and energy spectra, a representative test was conducted. This test aimed to determine whether the wave fields measured during the four-month period could be extrapolated to analyze long-term wave fields, as outlined in Section 4.2. This precaution was necessary since LSTM models tend to lack generalization ability for scenarios that were not part of the training dataset, which is a common limitation of purely data-driven models.

2.2.1. Wind and water level data

The wave development within an estuary is widely acknowledged to be influenced by two factors: the wind field and water depth. In the case of finite depth conditions, wave height is known to be constrained (Karimpour et al., 2017). To effectively model wave parameters and energy spectra, this study incorporated wind and water level data as input features for the LSTM models. The water level data were obtained from NOAA 8571421, located at Bishops Head, approximately 21.3 km north of Fog Point. As for the wind data, it was sourced from four dispersed NOAA stations across the bay: 8571421 at Bishops Head, 8635750 at Lewisetta, 8632837 at Front Range, and 8638901 at Chesapeake Channel. These stations were carefully chosen to encompass the large variation in wind fields observed within the large bay area. Both the geographic locations and data availability were taken into account during the station selection process. The wind roses derived from the measurements at these stations exhibit notable spatial heterogeneity in wind fields across the Chesapeake Bay (Fig. 2), which further supported the inclusion of wind data from all four stations as input features.

2.2.2. LSTM model setup

Previous studies have utilized past wave measurements, such as wave parameters recorded 3 or 6 h earlier, as input features for training LSTM models to forecast wave characteristics (e.g., Fan et al., 2020; Wei, 2021). However, this study does not incorporate previous wave measurements as input features during LSTM training. The reason for this omission is that the measured wave parameters were obtained from temporary wave gages deployed in 2020, rather than a permanent station. Consequently, including previous wave parameters as input features would render the developed models unsuitable for predicting waves in the future, or wave hindcast, such as in 2021, due to the

unavailability of wave measurements from that year. Essentially, this study focuses on constructing cause-effect wave models by solely applying forcing functions (e.g., wind and water level data) to predict wave parameters and energy spectra (Londhe and Panchang, 2018). Given the typically continuous availability of wind data, the input features in this study encompassed both the current wind data and the wind data recorded 1 h, 2 h, and 3 h prior, accounting for the time required for wave growth along the wind fetch. We further examined whether the inclusion of past water level data as input features could enhance the accuracy of the models. The findings indicated that the model accuracy remained comparable to the one achieved when using solely the current water level data as an input feature. Therefore, the developed LSTM models in this study employed the current and previous 3 h of wind data, along with the current water level, as the input features to predict wave parameters and energy spectra of the current state.

In this study, the input features used to estimate wind waves included wind and water level data. Specifically, the hourly u- and vwind velocity components and water levels measured at NOAA station 8571421 were utilized to predict the local water depth (d) at each wave gage location. This information was then employed to calculate wave power in this study. To model H_{m0} , a network was developed using the wind data from all four NOAA stations and the water level data from NOAA station 8571421 as input features. Since $H_{\rm m0}$ is important for predicting T_p , it was applied as an input along with wind and water levels in the T_p prediction. To simulate energy spectra E in the frequency domain, the inputs included wind, water level, $H_{\rm m0}$, and $T_{\rm p}$. The loss function for the complete network was determined by summing the error functions of d, $H_{\rm m0}$, $T_{\rm p}$, and E. Fig. 3 and Table 1 show the architecture of composite networks, as well as input features and labels. Although it was possible to use independent networks to predict d, H_{m0} , $T_{\rm p}$, and E separately, this approach was not employed in this study to avoid the potential propagation of errors from one network to another.

The composite LSTM models were tested and validated using hourly datasets from 03/07/2020 to 03/15/2020 and 03/01/2020 to 03/07/2020, respectively. The training data encompassed the remaining dataset in 2020. The development of LSTM models involved the utilization of PyTorch. The training procedure aimed to minimize the mean square error (*MSE*) for simulating wave parameters and spectra

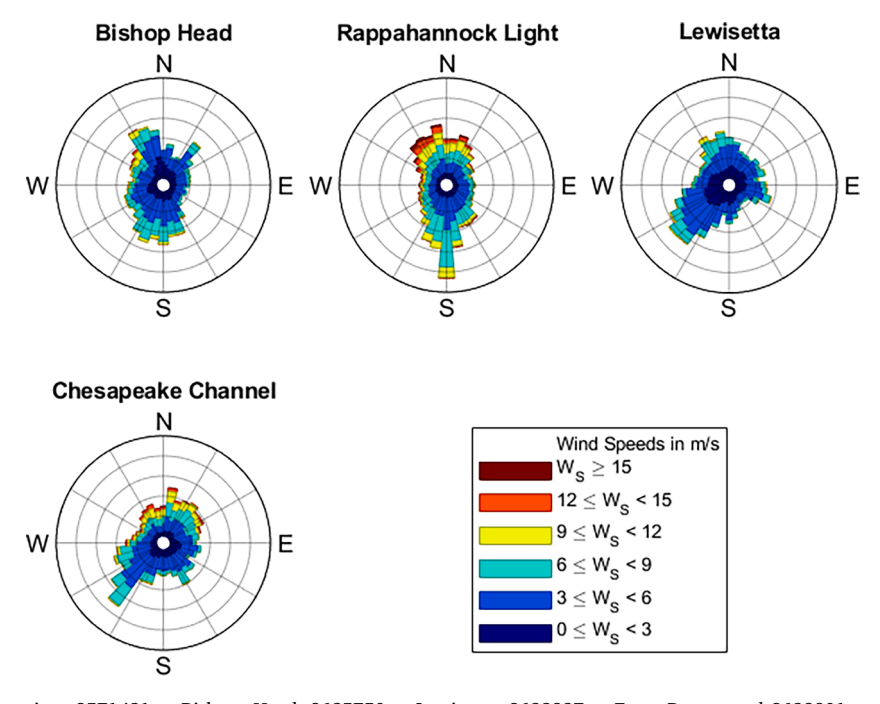


Fig. 2. Wind roses at NOAA stations 8571421 at Bishops Head, 8635750 at Lewisetta, 8632837 at Front Range, and 8638901 at Chesapeake Channel based on measurements from 2020 to 2022.

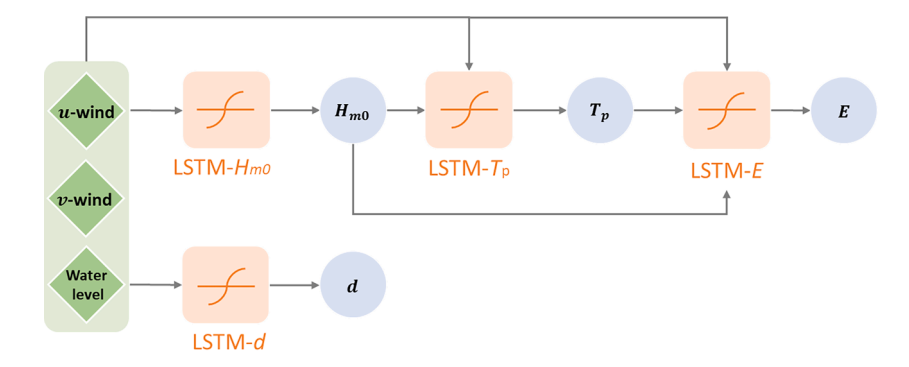


Fig. 3. A diagram showing the design of the LSTM models used to estimate d, $H_{\rm m0}$, T_p , and E. The 'S' marker in the orange box represents hyperbolic tangent functions (the activation function).

Table 1
Input features and labels to estimate wave parameters and spectra using LSTM models.

Targets	Input features	Labels
d	<i>u</i> - and <i>v</i> -wind speed and water level data at NOAA stations 8571421	Measured d
$H_{ m m0}$	u- and v-wind speed data at NOAA stations 8571421,	Measured
	8635750, 8632837, and 8638901, water level data at	$H_{ m m0}$
	NOAA station 8571421	
$T_{ m p}$	u- and v-wind speed data at NOAA stations 8571421,	Measured T_p
	8635750, 8632837, and 8638901, water level data at	
	NOAA station 8571421, predicted $H_{\rm m0,in}$	
E	u - and v -wind speed data at NOAA stations 8571421, 8635750, 8632837, and 8638901, water level data at NOAA station 8571421, predicted $H_{\rm m0}$ and $T_{\rm p}$	Measured E

(Table A1). The training process continued until the MSE for d, H_{m0} , $T_{\rm p}$, or E ceased to decrease. The LSTM models had a sequence length of 16 and utilized the sigmoid and hyperbolic tangent functions as the gating and output activation functions, respectively (Hochreiter and Schmidhuber, 1997). The weights and biases were initialized using a uniform distribution ranging from $-\sqrt{K}$ to \sqrt{K} , where K is calculated as 1 divided by the number of nodes. Normalization techniques were applied to ensure inputs and outputs fell within the range of -1 to 1, thereby

mitigating the impact of variations in parameters. The Adam optimization algorithm was employed for network training (Kingma and Ba, 2014), with an initial learning rate of 0.01. The training process was performed on a system equipped with an Intel Core i7 processor and 32 GB memory, taking approximately 30 s to complete.

To identify the most suitable network structures for predicting wave parameters and spectra at each wave gage location (Wang et al., 2022c, 2023b), a thorough examination of 156 structures was conducted. These structures encompassed 1 to 4 hidden layers, each with 2 to 40 nodes. The performance of different structures was quantified using a composite performance score, including bias, SI, and R^2 (Table A1). The structure with the highest score was considered the optimal choice (Table A2).

3. Results

3.1. Measured wave characteristics

The time series of measured d, H_{m0} , and T_p at WG3, WG4, and WG5 are shown in Figs. 4, A1 and A2 (in the appendix), respectively. It should be noted that the wave data collected at WG5 after May 11 had poor quality, so the data were excluded from further analysis in this paper. The comparisons of H_{m0} and T_p at three gages are presented in Fig. 5. As expected, the H_{m0} at WG3 (offshore location) was the highest, while the H_{m0} at WG4 protected by structures was the lowest among the three gages. The T_p values at WG3 and WG5 (embayment location) are similar,

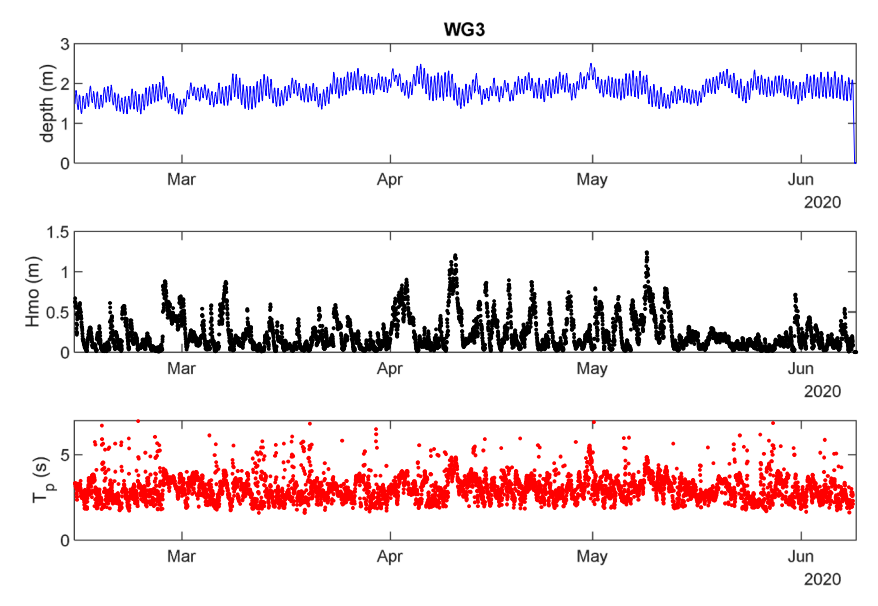


Fig. 4. Time series of measured d, $H_{\rm m0}$, and T_p at WG3.

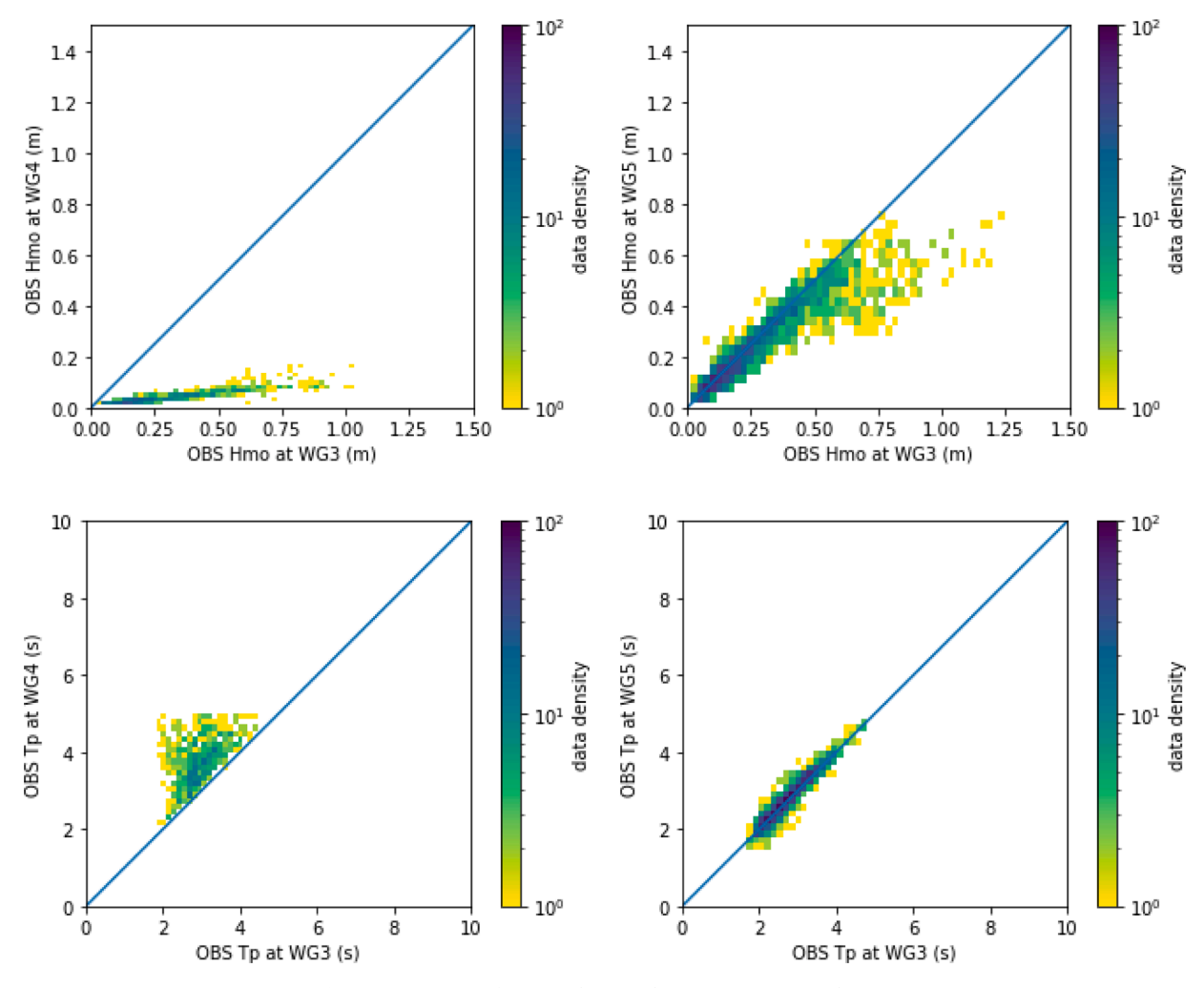


Fig. 5. Comparison of measured $H_{\rm m0}$ and T_p at WG3, WG4, and WG5.

which are generally smaller than those observed at WG4, indicating short waves were dissipated more by the low-crested breakwater. Throughout the deployment period, the average $H_{\rm m0}$ measured at WG3, WG4, and WG5 were 0.28 m, 0.04 m, and 0.25 m, respectively. The averaged $T_{\rm p}$ measured were 2.77 s, 3.85 s, and 2.78 s at WG3, WG4, and WG5, respectively. The decrease in wave height observed from WG3 to WG4 may be attributed to a combination of factors, including bathymetry (wave breaking due to varying depths), bottom friction, and the presence of breakwaters (Wang et al., 2022c).

For the measured wave spectra (*E*), several energy densities (with the peak energy density $E_{max} > 0.1 \text{ m}^2/\text{Hz}$ at WG3) are shown as examples in Fig. 6. It was found that the energy spectra recorded at WG4 were much lower than those recorded at WG3 and WG5, attributed to the dissipation caused by the depth-limited wave breaking, bottom friction, and structures. Interesting to see is that the energy spectra at low frequencies (f < 0.015 Hz) at WG4 exhibited similar magnitudes to those at WG3, indicating that subharmonic waves may propagate over the structures without experiencing significant damping effects. Moreover, the peak wave frequency (f_p) at WG4 is no greater than the ones at WG3 and WG5, consistent with the previous observations of T_p . Because of the wave-wave triad interactions (Zhu et al., 2020), two spectral peaks with frequencies of f_p and $2f_p$ can be observed at WG3 and WG5 (e.g., Feb 27 2020 07:00:00). These peaks align with the primary waves and their higher harmonics, respectively. It was found that the observation of high harmonics was more frequent when $k_p d$ (Kp is the wave number) smaller than 1 and 0.8 at WG3 and WG5, respectively. The occurrence of these high harmonics accounted for 27 % and 48 % of all wave measurements during the deployment period at WG3 and WG5, respectively. Fig. 7(a) shows the wave spectra normalized by f_p at each gage location averaged over the entire deployment period. At both WG3 and WG5, two spectral peaks are visible in sea wave band, although the feature at WG5 is more pronounced, consistent with the analysis presented earlier. Fig. 7(b) offers a zoomed-in view of the averaged wave spectra with the same vertical axis, highlighting the details of the infragravity waves (IG waves). It is evident that IG waves were present at all three gages with the same order of magnitude. The peak energy of the IG waves at different gages follows this order: $IG_{WG5} > IG_{WG4} >= IG_{WG3}$. The higher IG energy observed at WG5, compared to WG3, can be attributed to the energy transfer from the short waves to the IG band during wave shoaling and the varying breaking locations. The breakwaters leads to a significant reduction in short-wave energy, yet the IG wave energy at WG4 remains comparable to that at WG3. We think that the IG waves at WG4 mainly stem from the interplay of breaking and wave groups during wave overtopping and the energy transfer from higher to lower frequency bands over the mud flat located seaward of the breakwaters. Although resonance could occur between the shoreline and the breakwaters, given the short distance, the existence of vegetation, and a sloping seabed, it is unlikely to happen in this scenario. Further studies using numerical models, such as Funwave-TVD, could be carried out to test the hypothesis.

3.2. Prediction of integral wave parameters and energy density spectra

Fig. 8 presents the comparisons of d, H_{m0} , and T_p between the LSTM-

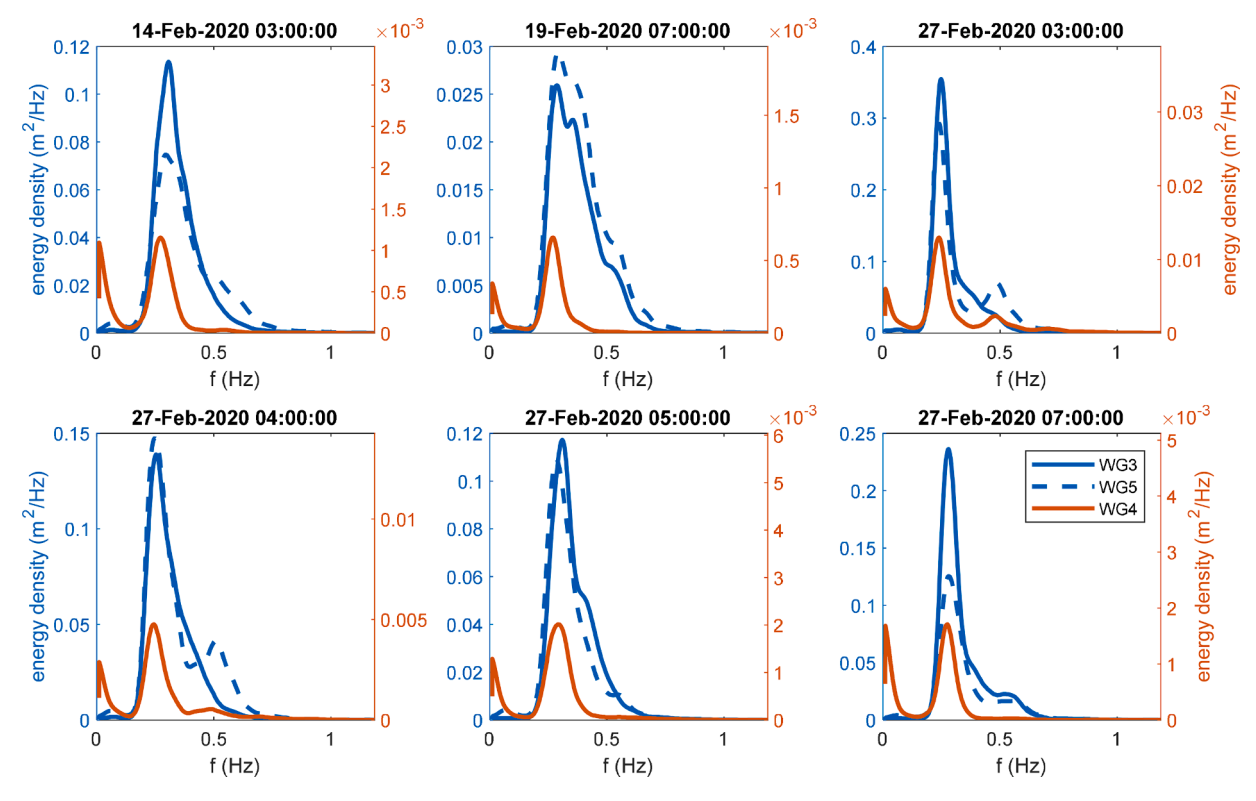


Fig. 6. Measured spectra at WG3, WG4, and WG5 at selected time slots.

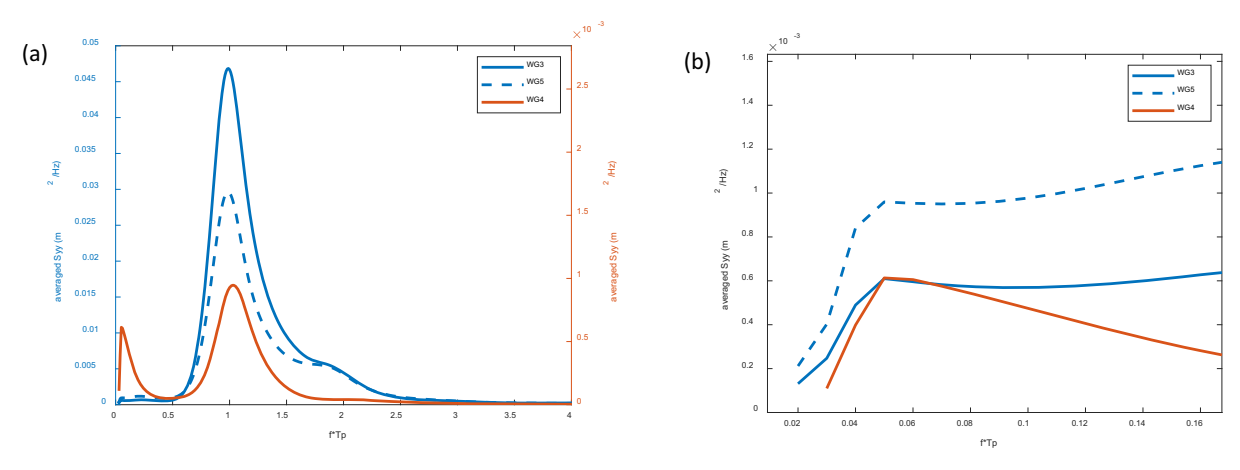


Fig. 7. Averaged wave spectra at WG3, WG4, and WG5 for the entire deployment duration. (a) full spectra (WG3 and WG5 use the left vertical axis, and WG4 uses the right axis); (b) Low-frequency bands (same vertical axis for all three gages).

predicted and observed values during the testing phase. The composite wave models demonstrate strong predictive abilities in estimating $H_{\rm m0}$ at WG3 and WG5, exhibiting R^2 values of approximately 0.84 and RMSE of around 0.07 m. Similarly, the prediction precision for $T_{\rm p}$ at WG3 and WG5 also quite satisfactory, with R^2 values about 0.80 and RMSE about 0.27 s. As the training data at WG4 are much fewer than the ones at WG3 and WG5, the estimated wave parameters are less accurate than the ones at WG3 and WG5, especially for predicting $T_{\rm p}$. However, it is worth mentioning that many existing data-driven wave models have difficulty predicting $T_{\rm p}$ and are mostly only focused on predicting $H_{\rm m0}$.

The developed networks in this study also generate predictions of frequency spectra. The comparison of the estimated and observed spectra at each wave gage can be found in Fig. 9. The findings demonstrate a significant level of agreement between the model results and the field measurements, with R^2 values of about 0.69. Some examples of

comparison between measured and estimated spectra values at WG3 and WG4 (with high energy) are shown in Fig. 10. To further determine the model performance for estimating energy spectra, extra parameters were computed to investigate the discrepancies between the measured and simulated energy spectra. These parameters encompass the peak energy density ($E_{\rm max}$) and zero moment of the wave power spectra (m_0). $E_{\rm max}$ serves as an indicator of the peak wave spectral density in the frequency domain and has been previously explored in studies conducted by Dabbi et al. (2015) and Wang et al. (2023b). m_0 is defined as

$$m_0 = \int\limits_f^{f_{
m max}} S_{yy}(f) df$$
, which shows the area under the spectral curve. To

better examine the prediction skill of the developed models, the spectra were separated into two parts by the $f_{\text{sep}} = 1.5/T_{\text{p}}$, and $m_{0, left}$ and

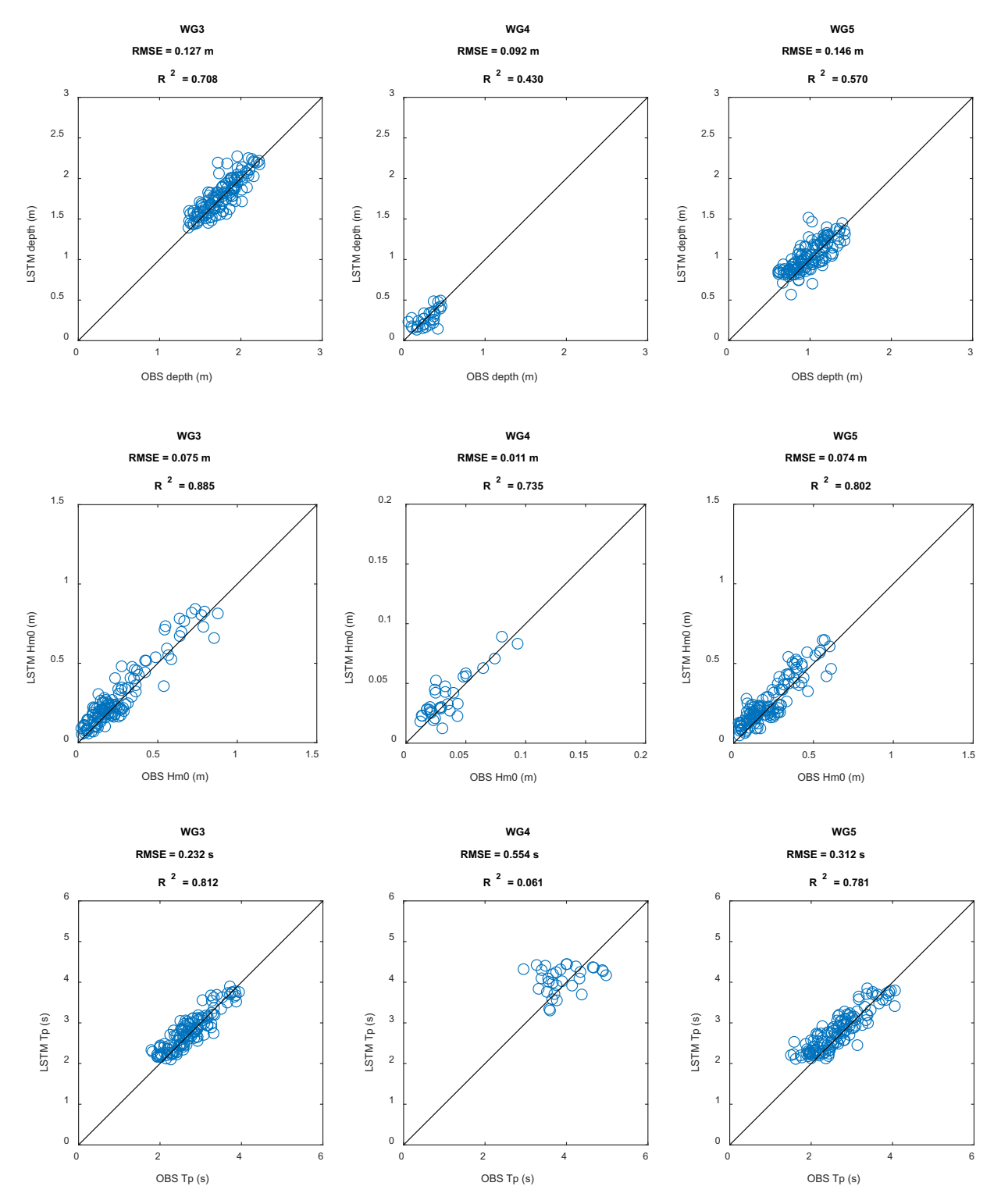


Fig. 8. Comparison of measured and predicted d, H_{mo} , and T_p at each gage location (testing data only).

 $m_{0, right}$ were calculated as $m_{0, left} = \int\limits_{f_{min}}^{f_{sep}} S_{yy}(f) df$ and $m_{0, right} = \int\limits_{f_{max}}^{f_{max}} S_{yy}(f) df$, respectively. $f_{sep} = 1.5/T_p$ was set as the threshold in this

study, because $f \times T_p = 1.5$ correlates to the separation of the two harmonics at WG3 and WG5, as shown in Fig. 7. By comparing the predicted

and observed spectra to the left and right of the thresholds (i.e., $m_{0, left}$ and $m_{0, right}$) separately, we can investigate the model performance on predicting low and high harmonics on the wave energy spectra more clearly. The time series of predicted and measured E_{\max} , $m_{0, left}$, and $m_{0, right}$ are shown in Fig. 11. The good agreement observed in these results further indicates the high accuracy of the composite models in predicting wave spectra at the study site.

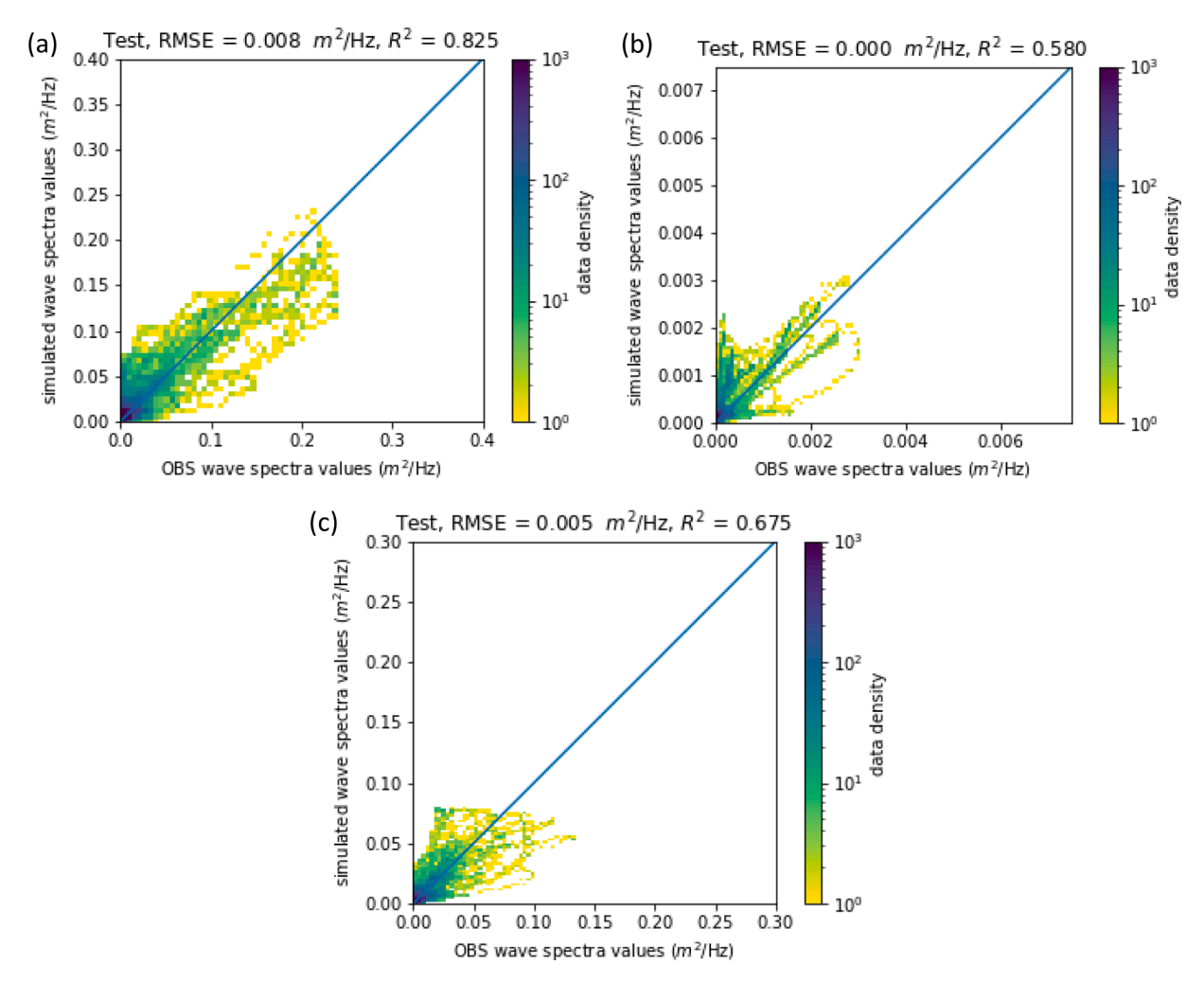


Fig. 9. Comparison of measured and predicted wave spectra at (a) WG3, (b) WG4, and (c) WG5 (testing data only).

4. Discussion

4.1. Transfer learning for predicting spectra at WG5

Normally, the neural networks are trained from scratch (e.g., initialized with uniform distribution in this work), while transfer learning utilizes pretrained networks to initialize the subsequent predictions. By doing so, transfer learning can expedite the training process and enhance prediction accuracy, when the upcoming prediction involves slightly altered wave boundary conditions or bathymetry (e.g., Kissas et al., 2020). In this study, the measured integral wave parameters present some similar patterns at WG3 and WG5 (Fig. 5), and the measured energy spectra at both gages show energy transfer to higher harmonics owing to triad wave-wave interactions (Fig. 7). Therefore, to better capture the secondary peaks in the wave spectra at WG5, we developed a pretrained model at WG3 only using the training data with $k_p d < 1$ (i.e., at low tides or shallow water depths, when significant cross-spectral energy transfers to higher harmonics were observed at WG3). The pretrained model at WG3 was then used to initialize the model training at WG5. Afterward, the parameters of the second network were fine-tuned using the training data specifically from WG5. This process led to an enhancement in the prediction accuracy and computational efficiency for subsequent predictions at WG5.

Fig. 12 presents examples of estimated wave spectra at WG5, comparing the results obtained with and without the utilization of transfer learning. The findings demonstrate that the composite models incorporating transfer learning exhibit better prediction performance.

Moreover, when employing transfer learning, the loss function converges after approximately 100 iterations, which is faster compared to the model without transfer learning, requiring approximately 300 iterations. This improvement in convergence speed can be attributed to the similarity in wave boundary conditions and bathymetry between WG3 and WG5. Consequently, initializing the network parameters at WG5 with the pretrained model from WG3 leads to enhanced prediction skills and accelerated convergence.

4.2. Wind field representativeness during deployment

This section shows a representative test for assessing the suitability of using models trained with measured wave parameters from February to May 2020 for predicting long-term wave processes. The importance of this test lies in the fact that purely data-driven models, such as LSTM, often face challenges in accurately predicting scenarios that were not included in the training dataset. To assess the representativeness of the wave generation forcing, the following procedures were implemented as outlined by Wang et al. (2022b). First, hourly wind direction and wind speed datasets were partitioned into 36 directional bins with 10° intervals (i.e., 0-10, ..., 350-360) and 50 speed bins with 0.5 m/s intervals (i.e., 0-0.5, ..., 24.5-25 m/s) for both the four-month period in 2020 and the years of 2020, 2021, and 2022. This division process resulted in a total of 1800 divisions (i.e., $36\times 50=1800$). In order for a wind forcing to be considered representable by the four-month data, it must fall within one of the divisions shared by the four-month data (Fig. 13). It was found that, on average, 95.5 % of the wind conditions

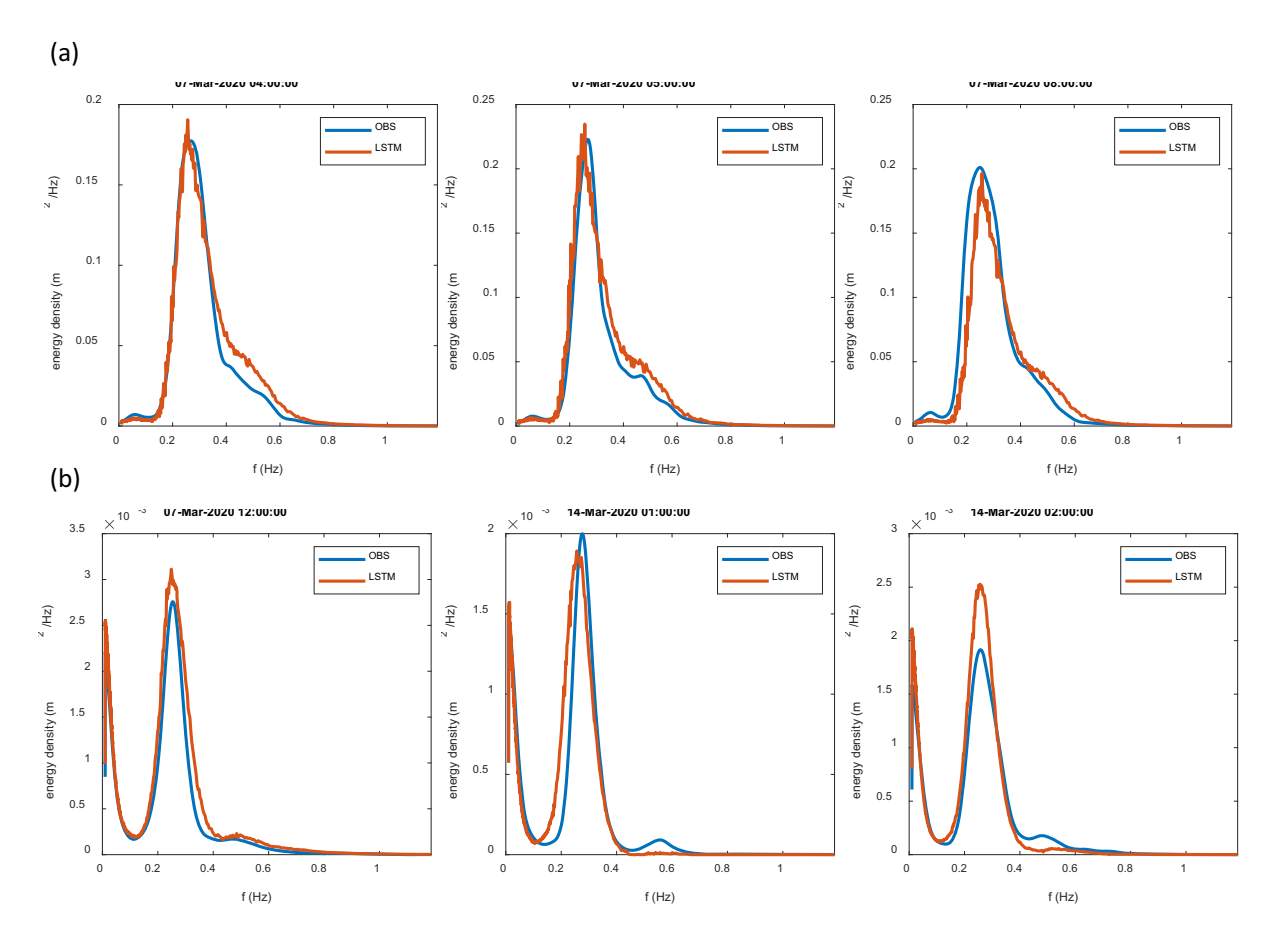


Fig. 10. Comparison of measured and predicted wave spectra at (a) WG3 and (b) WG4 at specific instances during the testing period.

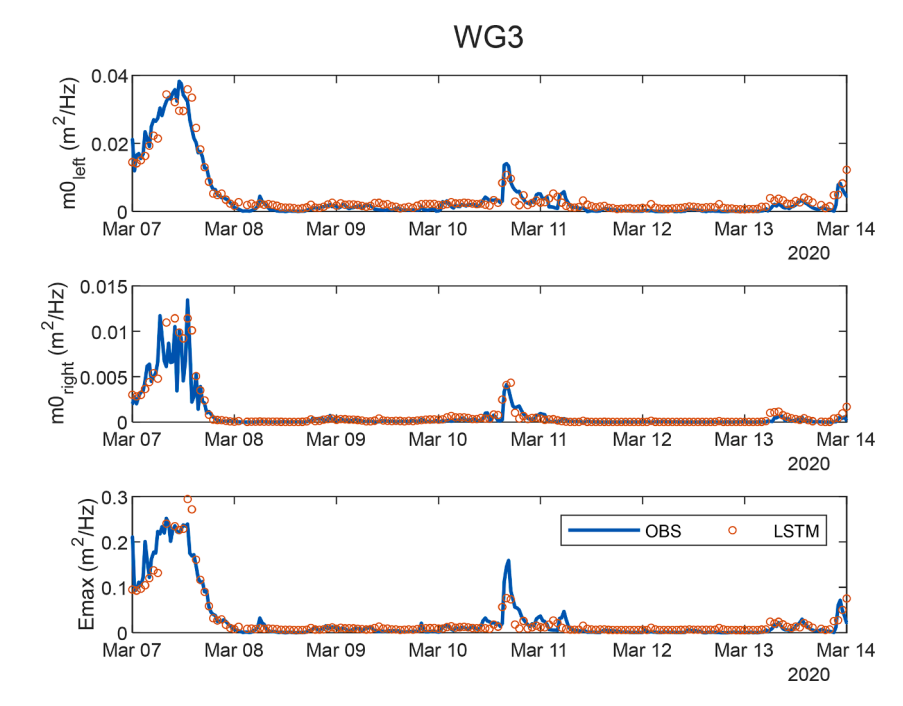


Fig. 11. Time series of observed and predicted m_0 and $E_{\rm max}$ at WG3 (only contain the testing data).

recorded at the four stations between 2020 and 2022 could be represented by the wind conditions observed during the four-month period in 2020 (Table 2). Hence, given that the majority of the wind conditions

over the three-year period could be represented by the wind conditions from February to May 2020, the measured wave parameters were employed in this study to build LSTM models for predicting wave spectra

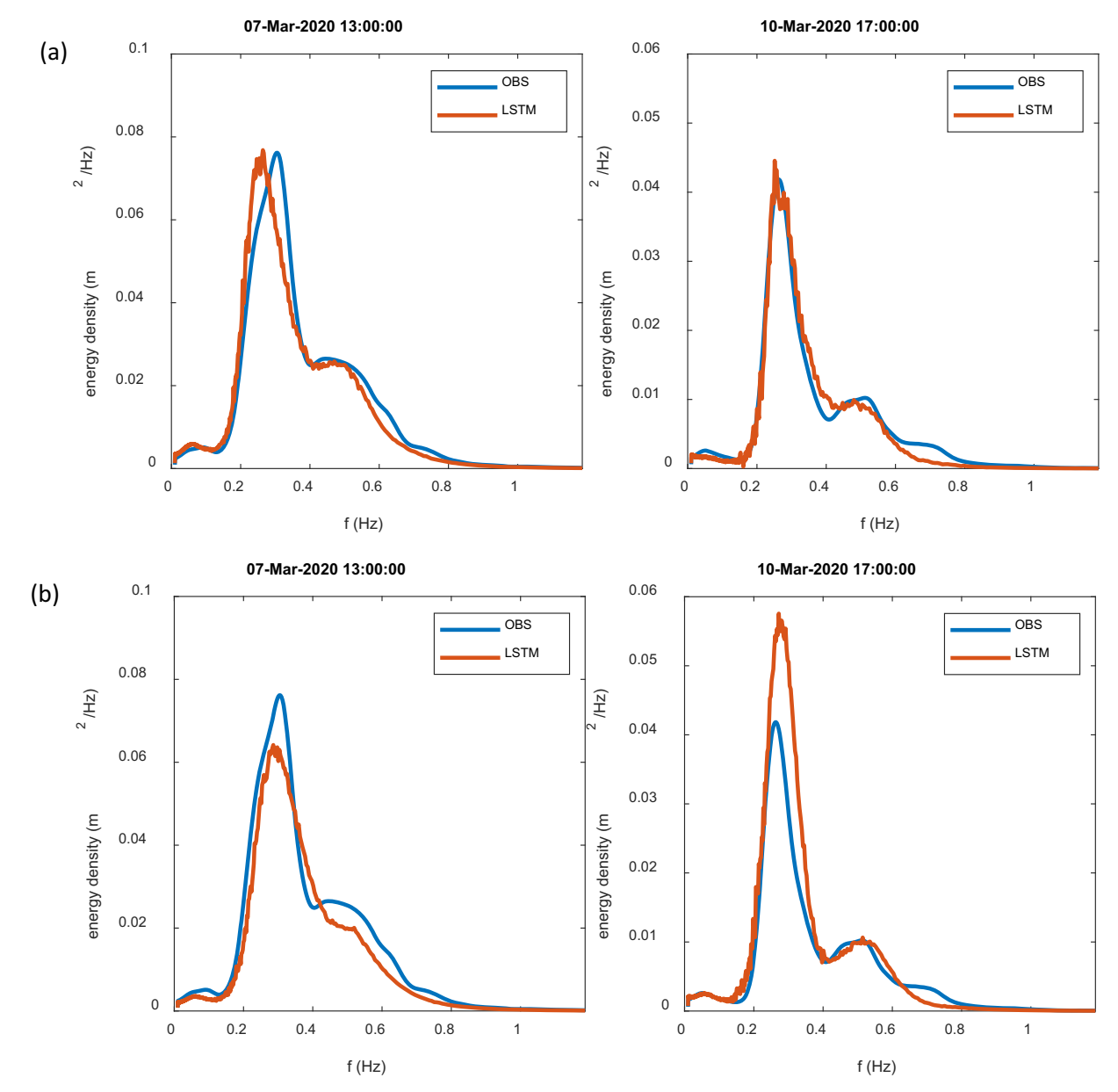


Fig. 12. Comparison of measured and estimated wave spectra at WG5 (a) with and (b) without transfer learning.

and parameters in 2020, 2021, and 2022.

4.3. Wave power computed by spectra and integral wave parameters

During storms and hurricanes, the wave environment in the estuary can be complicated due to the swift changes in wind fetch and wind speed. Thus, the integral wave parameters, such as H_{m0} and $T_{\rm p}$, may not be applied to determine the wave power changes nearshore adequately. By contrast, wave spectra can better reveal the energy changes in different frequency bands when waves propagate to shorelines. In this section, we evaluated the differences between the wave power computed using integral parameters and spectra at the study site in 2020, 2021, and 2022.

To determine the wave power in a narrow-banded spectrum, the wave power can be calculated by the integral wave parameters and local water depth as

$$P_{parameter} = \frac{\rho g H_{m0}^2}{16} c_g \tag{1}$$

where, c_g is wave group velocity and ρ is water density. For a complex wave field with multiple spectral peaks or a broad spectral shape, the wave power can be better calculated based on the spectra directly as

$$P_{spectra} = \rho g \int c_g E(f) df \tag{2}$$

The results indicate that the estimated wave power based on spectra was higher than the values calculated based on integral parameters at WG3, WG4, and WG5 over the three-year period. For instance, in 2020, the annual wave power calculated based on wave spectra at WG3, WG4, and WG5 was 188.7 W/m, 1.33 W/m, and 90.6 W/m, respectively. However, when the wave power was computed based on the integral parameters, these values decreased to 148.5 W/m, 1.28 W/m, and 78.0 W/m. To better understand the differences in wave power computed using two different approaches, the proportion and discrepancy of wave power determined by integral parameters and spectra were computed (Fig. 14). It can be observed that the wave powers calculated based on integral wave parameters are lower than those calculated using spectra, especially at WG3 and WG5 (the difference can go up to 448 W/m and

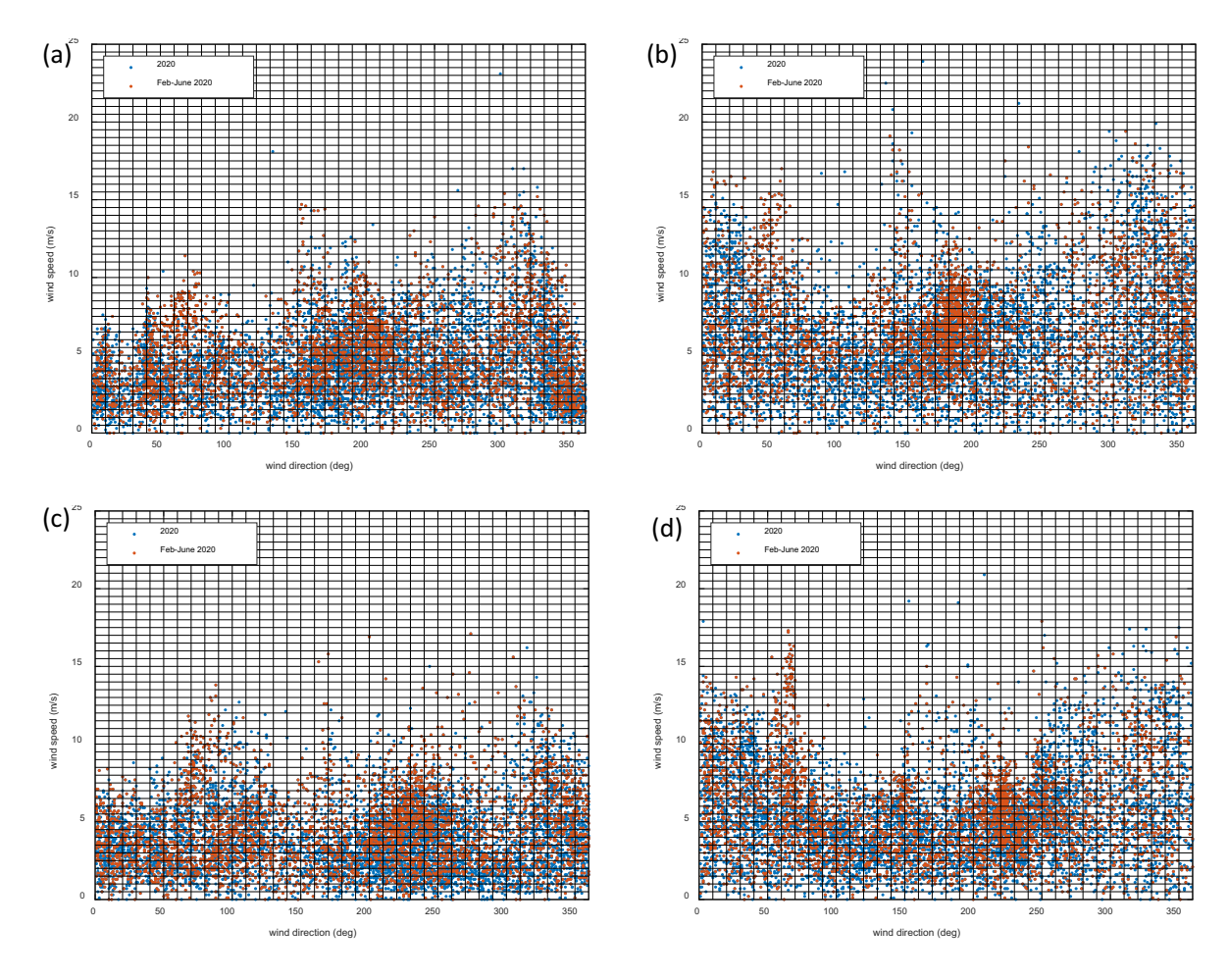


Fig. 13. Hourly data of measure wind speed and direction at (a) Bishops Head (8571421), (b) Front Range (8632837), (c) Lewisetta (8635750), and (d) Chesapeake Channel (8638901) in 2020 versus February to June 2020.

Table 2The percentages of wind data from various years that can be captured by the four-month data in 2020.

Year	Bishops head (8571421)	Front range (8632837)	Lewisetta (8635750)	Chesapeake channel (8638901)
2020	97.8 %	95.9 %	98.0 %	95.9 %
2021	98.1 %	95.3 %	93.5 %	95.2 %
2022	94.7 %	92.9 %	96.1 %	93.0 %
Average	96.9 %	94.7 %	95.8 %	94.7 %

103 W/m at WG3 and WG5, respectively), where the wave energy is relatively high. The mean values of $P_{spectra}/P_{integral}$ and abs $(P_{spectra}-P_{integral})$ at WG5 are 1.3 and 13.0 W/m, respectively, and these values increase to 1.4 and 40.5 W/m at WG3. This indicates that using integral parameters to obtain wave power can result in an even greater underestimation of wave power with larger waves.

Using wave spectra to compute wave power has an implication for marsh edge stability analysis. There is a linear relationship between the rate of salt marsh edge erosion and the annual wave power of wind waves (Leonardi et al., 2016). Taking the wave conditions at WG5 in 2020 as an example, if the wave power and marsh edge retreat rate were calculated based on the integral wave parameters (78.0 W/m) instead of the wave spectra (90.6 W/m), there would be an approximate 16 % underestimation of shoreline retreat at the study site. Therefore, it is

recommended that wave spectra be used to compute wave power for shoreline erosion prediction and for design of flood protection structures, particularly under energetic storm conditions.

The wave power calculated from LSTM-predicted wave spectra from 2020 to 2022 is presented in Table 3. On average, the wave power was 194.1 W/m, 1.3 W/m, and 92.8 W/m at WG3, WG4, and WG5 over the three years, respectively. It is worth mentioning that during the field experiments between February and May 2020, the measured wave powers were higher, with values of 211.0 W/m, 1.4 W/m, and 99.3 W/m at WG3, WG4, and WG5, respectively. This can be attributed to the energetic wave conditions in the stormy months when the experiments took place. Specifically, the wave climate during late winter and spring was more severe than that over the entire year, leading to higher observed wave power levels over the four-month period.

4.4. Implications to living shoreline sustainability

In these living shorelines with bay beaches, headland breakwaters, and marsh planting, the wave energy reduction by the breakwaters is considerable (i.e., WG3 vs. WG4), while the wave energy in the bay remains constantly lower than the offshore under energetic wave conditions due to wave breaking and wave refraction (i.e., WG3 vs. WG5). However, the annual wave power in the bay between two headland breakwaters remains very high (> 90 w/m) in this energetic wave environment. Because of a lack of sandy material in the study site to form a stable beach, as seen from historical aerial images, significant

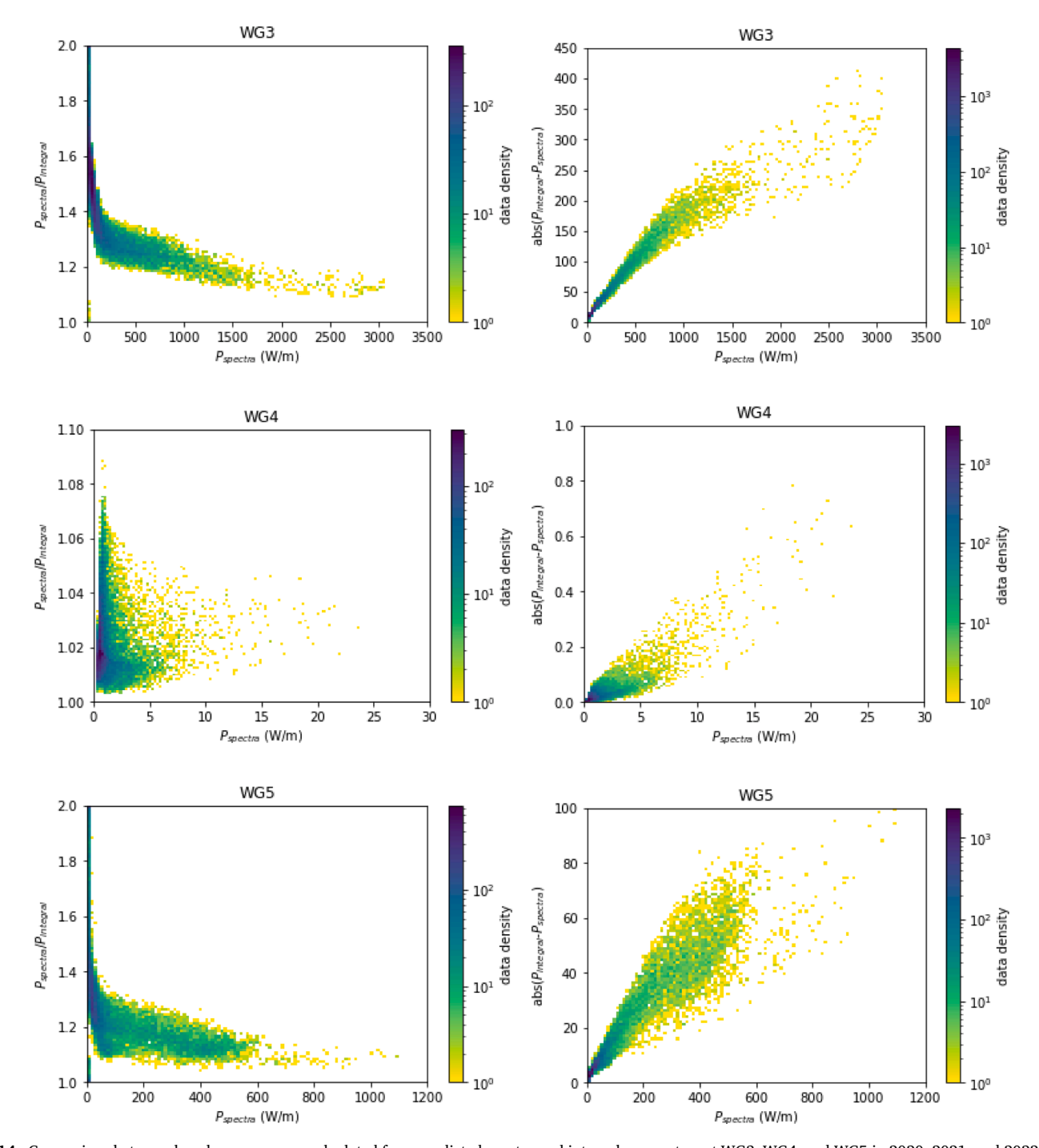


Fig. 14. Comparison between hourly wave power calculated from predicted spectra and integral parameters at WG3, WG4, and WG5 in 2020, 2021, and 2022. Left: Ratios of wave power computed by spectra and integral parameters as a function of wave power; Right: Differences in wave power computed by two different methods.

Table 3 Annual average wave power at WG3, WG4, and WG5 in 2020, 2021, and 2022 (unit: W/m).

	WG3	WG4	WG5
2020	188.7	1.3	90.6
2021	187.2	1.3	91.8
2022	206.4	1.3	96.1

marsh edge erosion is expected to continue based on the relationship between annual wave power and marsh edge retreat rate (Leonardi et al., 2016) and an analysis of aerial imagery between 2016 and 2022 (Wang et al., 2023b). Thus, a secondary sill structure would be needed to further reduce the wave power near the shoreline in the bay between two headland breakwaters to protect the marsh edge.

Although the considerable wave power reduction from WG3 to WG4 was observed over the four-month field experiments and predicted by the LSTM models over three years, it may not necessarily result in sediment deposition and marsh accretion for the salt marshes behind the breakwaters. Marsh erosion is still possible due to the limited sediment supply from marine sources, as well as the impacts of circulation and

current velocity behind the headland breakwater on the settling and deposition of suspended sediments. Furthermore, marine sediments are likely blocked by the breakwaters with a relatively high crest elevation, except during storms when waves can overtop the breakwaters and carry sediments to the tidal flat and salt marshes behind it. Therefore, an application of external sources of sediments, such as dredging materials, may be needed to supplement sediments for marsh accretion both laterally and vertically. Marsh planting can be another critical component of this type of living shoreline structure. Overall, to promote sustainable living shoreline development, in addition to reducing wave energy, it is important to maintain the physical conditions, such as ensuring inundation duration at marsh surface elevation to promote vegetation growth and trap inorganic sediments.

5. Conclusions

Rock breakwaters, sand nourishment, and planting of salt marsh species as living shoreline structures were constructed along the Fog Point shoreline in Martin National Wildlife Refuge, Maryland, in 2016 in response to the impact of Superstorm Sandy (2012) and future storms. To assess the influence of the living shoreline structures in mitigating wave energy, wave gages and current meters were deployed seaward and shoreward of the structures from February to May 2020. The paper introduces a new framework for constructing surrogate models that accurately predict wave frequency spectra and integral wave parameters, employing the LSTM algorithm with minimal computational requirements. This approach enables us to better comprehend the fluctuation in wave power surrounding the living shoreline structures ranging from hours to years. Our findings contribute to the development of effective and efficient methods for predicting wave energy and assessing the efficacy of living shoreline structures for coastal protection and habitat enhancement.

In this research, we presented field observations of wind waves based on four-month in-situ measurements and developed composite LSTM models to estimate long-term spectral wave evolution along the living shoreline structures at Fog Point. As the estuarine wind fields showed significant variability, we employed wind data from four NOAA stations, namely 8571421 at Bishops Head, 8635750 at Lewisetta, 8632837 at Front Range, and 8638901 at Chesapeake Channel, as input features to the machine learning algorithms. The novel composite LSTM wave models exhibited a notable level of accuracy in predicting $H_{\rm m0}$ at WG3 and WG5, with R^2 values of about 0.84 and RMSE of about 0.07 m. Similarly, the models exhibited satisfactory accuracy in simulating T_n at WG3 and WG5, with R^2 values around 0.80 and RMSE of approximately 0.27 s. As the amount of training data at WG4 was much less than that at WG3 and WG5, the estimated wave parameters at WG4 were less accurate, particularly for simulating T_p . Moreover, the composite networks were able to generate predictions of wave frequency spectra, with R^2 values around 0.69. To better capture the secondary peaks in the wave spectra at WG5 and accelerate the convergence speed of training the ML models, the transfer learning method was employed to compute wave spectra based on data collected at WG3, given their similarity in wave boundary conditions and bathymetry.

To examine whether the models trained by the measured wave parameters can be used to predict long-term wave processes, a test was conducted to assess the representativeness of the wind data during the four-month period in 2020. On average, it was found that the fourmonth data from the four NOAA stations could represent approximately 95.5 % of the annual forcings in 2020, 2021, and 2022. With this validation, the developed LSTM models were employed to investigate the wave spectra and parameters around the structures throughout the years. Subsequently, the wave power variations along the structures were computed using the estimated wave parameters and energy spectra over the three-year period. The results revealed that the estimated wave power from spectra was higher than the values calculated based on

integral parameters at WG3, WG4, and WG5 from 2020 to 2022. This emphasizes the potential underestimation of wave power when relying solely on integral parameters in a complex wave field in the shallow water of an estuary, which could compromise the safety of engineering designs.

While this method offers predictions specific to a particular location, it serves as a valuable tool for quickly approximating long-term wave characteristics in scenarios requiring location-specific forecasts. It is important to note that the input parameters (e.g., wind and water level) must cover a sufficient duration to ensure that the training data accurately reflects wave conditions across multiple years. This is important because purely data-driven models often struggle with extrapolation tasks. A potential approach to address this challenge is to incorporate prior domain knowledge into machine learning techniques, such as the physics-informed neural networks introduced by Wang et al. (2022a). To sum up, this study introduces a new approach utilizing LSTM models to predict wave frequency spectra in estuaries. The results demonstrate that the proposed approach can provide an accurate and efficient estimation of wave spectra, making it a valuable tool for long-term wave forecasts or hindcasts. Additionally, it was found that relying solely on integral parameters may lead to an underestimation of the wave power of a complex wave field with multiple spectral peaks on broad spectra in shallow waters, highlighting the importance of considering wave spectra when assessing wave power and designing resilient shoreline structures. In closing, the findings presented in this study can be useful in assessing the effectiveness of the living shorelines in mitigating the impact of energetic wind waves. The methodology employed for modeling wave spectra and parameters can be extended to various coastal regions and

CRediT authorship contribution statement

Nan Wang: Methodology, Software, Data curation, Writing – original draft. Qin Chen: Conceptualization, Methodology, Investigation, Writing – review & editing, Supervision, Funding acquisition. Hongqing Wang: Investigation, Resources, Writing – review & editing. William D. Capurso: Investigation, Data curation, Writing – review & editing. Lukasz M. Niemoczynski: Investigation, Data curation, Writing – review & editing. Gregg A. Snedden: Investigation, Writing – review & editing.

Declaration of Competing Interest

The authors declare that they have no known competing financial interests or personal relationships that could have appeared to influence the work reported in this paper.

Data availability

Data will be made available on request.

Acknowledgments

This paper is based upon work supported in part by the National Fish and Wildlife Foundation (NFWF, Project #55032) and the National Science Foundation under Award No. 2139882. Any opinions, findings and conclusions or recommendations expressed in this paper are those of the authors and do not necessarily reflect the views of the National Science Foundation. Any use of trade, firm, or product names is for descriptive purposes only and does not imply endorsement by the U. S. Government. We thank Matt Whitbeck in the U.S. Fish & Wildlife Service, Chesapeake Marshlands National Wildlife Refuge Complex and Michael Brownley in the U.S. Geological Survey, Maryland-Delaware-D. C. Water Science Center for their assistance during the field deployment and retrieval of sensors. Data described in this paper are available in

Appendix

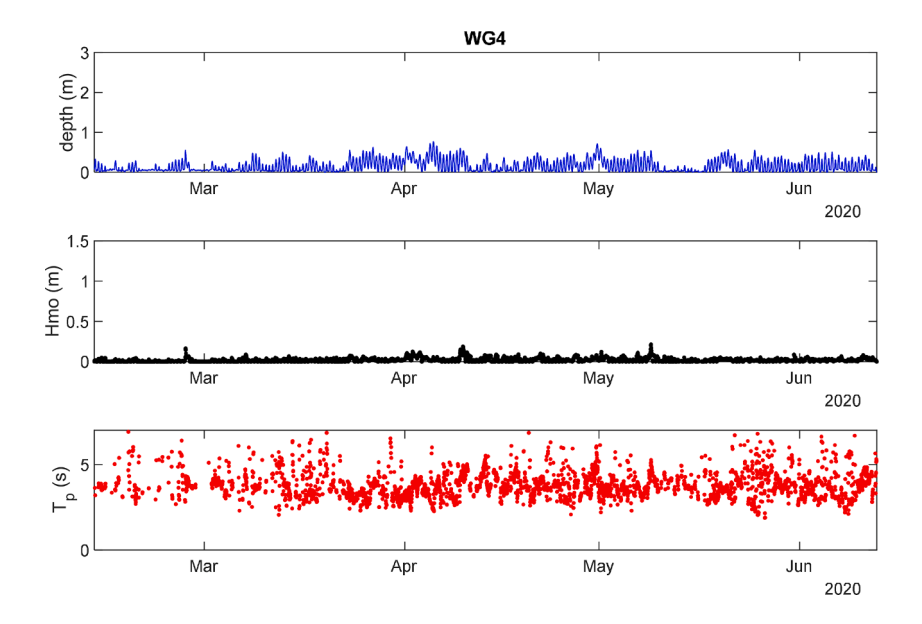


Fig. A1. Time series of measured water depth, $H_{\rm m0}$, and T_p at WG4.

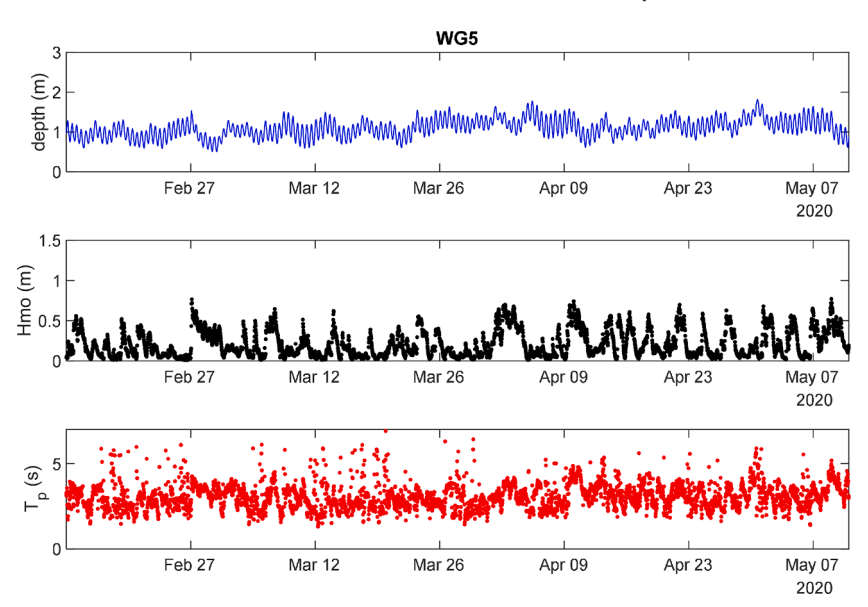


Fig. A2. Time series of measured water depth, $H_{\rm m0}$, and T_p at WG5.

Table A1
Statistical measures used in this study to evaluate the performance of the developed models.

MSE:	$MSE = \frac{\sum_{i}^{N} (y_i - \widehat{y_i})^2}{N}$
RMSE:	$RMSE = \sqrt{\frac{\sum_{i}^{N} (y_i - \widehat{y_i})^2}{N}}$
Scatter index (SI):	$SI = \frac{RMSE}{\overline{y}}$
bias:	$bias = \frac{1}{N} \sum_{i}^{N} \widehat{y_i} - y_i$
R^2 :	$R^{2} = \left(\frac{\sum_{i}^{N} (y_{i} - \widehat{y_{i}})^{2}}{\sqrt{\sum_{i}^{N} (y_{i} - y_{i})^{2} \sum_{i}^{N} (\widehat{y_{i}} - \widehat{y_{i}})^{2}}}\right)^{2}$
	(continued on next page)

Table A1 (continued)

Normalized SI performance:	$\widetilde{SI} = 1 - SI$
Normalized bias performance:	$\widetilde{Bias} = 1 - \frac{abs(bias)}{\overline{y}}$
Composite Performance Score:	$CPS = \frac{R^2 + \widetilde{SI} + \widetilde{bias}}{2}$
Total composite performance score:	$TCPS = \frac{1}{4}(CPS_d + CPS_{H_{mo}} + CPS_{T_p} + CPS_E)$

in which N is the number of samples, $\hat{y_i}$ is the estimated values, and y_i is the true value.

Table A2Optimal network structures applied in this study for estimating wave parameters and spectra at different gages.

		d	H_{mo}	$T_{ m p}$	Е
WG3	layer	1	2	1	4
	node	4	8	8	32
WG4	layer	2	2	2	4
	node	4	8	8	64
WG5	layer	1	2	1	4
	node	4	8	8	64

References

- Basco, D., 2020. Design of Coastal Hazard Mitigation Alternatives for Rising Seas. World Scientific.
- Bento, P.M.R., Pombo, J.A.N., Mendes, R.P.G., Calado, M.R.A., Mariano, S., 2021. Ocean wave energy forecasting using optimised deep learning neural networks. Ocean Eng. 219, 108372.
- Booij, N., Ris, R.C., Holthuijsen, L.H., 1999. A third-generation wave model for coastal regions: 1. Model description and validation. J. Geophys. Res. Ocean. 104, 7649–7666
- Dabbi, E.P., Haigh, I.D., Lambkin, D., Hernon, J., Williams, J.J., Nicholls, R.J., 2015. Beyond significant wave height: a new approach for validating spectral wave models. Coast. Eng. 100, 11–25.
- Elbisy, M.S., Elbisy, A.M.S., 2021. Prediction of significant wave height by artificial neural networks and multiple additive regression trees. Ocean Eng. 230, 109077.
- Fan, S., Xiao, N., Dong, S., 2020. A novel model to predict significant wave height based on long short-term memory network. Ocean Eng. 205, 107298.
- Filipot, J.-F., Cheung, K.F., 2012. Spectral wave modeling in fringing reef environments. Coast. Eng. 67, 67–79.
- Gao, S., Huang, J., Li, Y., Liu, G., Bi, F., Bai, Z., 2021. A forecasting model for wave heights based on a long short-term memory neural network. Acta Oceanol. Sin. 40, 62–69.
- Hao, W., Sun, X., Wang, C., Chen, H., Huang, L., 2022. A hybrid EMD-LSTM model for non-stationary wave prediction in offshore China. Ocean Eng. 246, 110566.
- Hardaway Jr, C.S., Gunn, J.R., 2010. Design and performance of headland bays in Chesapeake Bay, USA. Coast. Eng. 57, 203–212.
- Hochreiter, S., Schmidhuber, J., 1997. Long short-term memory. Neural Comput. 9, 1735–1780.
- Jörges, C., Berkenbrink, C., Stumpe, B., 2021. Prediction and reconstruction of ocean wave heights based on bathymetric data using LSTM neural networks. Ocean Eng. 232. 109046.
- Karimpour, A., Chen, Q., Twilley, R.R., 2017. Wind wave behavior in fetch and depth limited estuaries. Sci. Rep. 7, 40654.
- Kingma, D.P., Ba, J., 2014. Adam: a method for stochastic optimization. arXiv Prepr. arXiv1412.6980.
- Kissas, G., Yang, Y., Hwuang, E., Witschey, W.R., Detre, J.A., Perdikaris, P., 2020. Machine learning in cardiovascular flows modeling: predicting arterial blood pressure from non-invasive 4D flow MRI data using physics-informed neural networks. Comput. Methods Appl. Mech. Eng. 358, 112623.
- Leonardi, N., Ganju, N.K., Fagherazzi, S., 2016. A linear relationship between wave power and erosion determines salt-marsh resilience to violent storms and hurricanes. Proc. Natl. Acad. Sci. 113, 64–68.
- Londhe, S.N., Panchang, V., 2018. ANN techniques: a survey of coastal applications. Advances in Coastal Hydraulics 199–234.
- Luo, Q.-R., Xu, H., Bai, L.-H., 2022. Prediction of significant wave height in hurricane area of the Atlantic Ocean using the Bi-LSTM with attention model. Ocean Eng. 266, 112747.
- Marani, M., D'Alpaos, A., Lanzoni, S., Santalucia, M., 2011. Understanding and predicting wave erosion of marsh edges. Geophys. Res. Lett. 38, L21401.
- Mares-Nasarre, P., Molines, J., Gómez-Mart\\in, M.E., Medina, J.R., 2021. Explicit neural network-derived formula for overtopping flow on mound breakwaters in depth-limited breaking wave conditions. Coast. Eng. 164, 103810.
- McLoughlin, S.M., Wiberg, P.L., Safak, I., McGlathery, K.J., 2015. Rates and forcing of marsh edge erosion in a shallow coastal bay. Estuar. Coasts 38, 620–638.

- Meng, F., Song, T., Xu, D., Xie, P., Li, Y., 2021. Forecasting tropical cyclones wave height using bidirectional gated recurrent unit. Ocean Eng. 234, 108795.
- Meng, Z.-F., Chen, Z., Khoo, B.C., Zhang, A.-M., 2022. Long-time prediction of sea wave trains by LSTM machine learning method. Ocean Eng. 262, 112213.
- Miky, Y., Kaloop, M.R., Elnabwy, M.T., Baik, A., Alshouny, A., 2021. A recurrent-cascade-neural network-nonlinear autoregressive networks with exogenous inputs (NARX) approach for long-term time-series prediction of wave height based on wave characteristics measurements. Ocean Eng. 240, 109958.
- Ni, C., Ma, X., 2020. An integrated long-short term memory algorithm for predicting polar westerlies wave height. Ocean Eng. 215, 107715.
- O'Donnell, J.E.D., 2017. Living shorelines: a review of literature relevant to New England coasts. J. Coast. Res. 33, 435–451.
- Perini Management Services, 2014. Smith Island, Martin National Wildlife Refuge, Hurricane Sandy Resiliency Project #31, Fog Point Living Shoreline Restoration.
- Rijnsdorp, D.P., Reniers, A.J.H.M., Zijlema, M., 2021. Free infragravity waves in the North Sea. J. Geophys. Res. Ocean. 126, e2021JC017368.
- Sanford, L.P., Gao, J., 2018. Influences of wave climate and sea level on shoreline erosion rates in the Maryland Chesapeake Bay. Estuar. Coasts 41, 19–37.
- Sareen, K., Panigrahi, B.K., Shikhola, T., Nagdeve, R., 2023. An integrated decomposition algorithm based bidirectional LSTM neural network approach for predicting ocean wave height and ocean wave energy. Ocean Eng. 281, 114852.
- Schwimmer, R.A., 2001. Rates and processes of marsh shoreline erosion in Rehoboth Bay, Delaware, USA. J. Coast. Res. 17, 672–683.
- Ti, Z., Song, Y., Deng, X., 2022. Spatial-temporal wave height forecast using deep learning and public reanalysis dataset. Appl. Energy 326, 120027.
- Tolman, H.L., others, 2009. User manual and system documentation of WAVEWATCH III TM version 3.14. Tech. note, MMAB Contrib. 276.
- Wang, H., Chen, Q., Capurso, W.D., Wang, N., Niemoczynski, L.M., Whitbeck, M., Zhu, L., Snedden, G.A., 2023a. Field observation of wind waves and current velocity (2020) along the fog point living Shoreline, Maryland: U.S. Geological Survey data release, doi:10.5066/P9TXZX5W.
- Wang, N., Chen, Q., Chen, Z., 2022a. Reconstruction of nearshore wave fields based on physics-informed neural networks. Coast. Eng. 176, 104167.
- Wang, N., Chen, Q., Zhu, L., 2023b. Data-driven modeling of Bay-Ocean wave spectra at bridge-tunnel crossing of Chesapeake Bay, USA. Appl. Ocean Res. 135, 103537.
- Wang, N., Chen, Q., Zhu, L., Sun, H., 2022b. Integration of data-driven and physics-based modeling of wind waves in a shallow estuary. Ocean Model., 101978 https://doi. org/10.1016/j.ocemod.2022.101978.
- Wang, N., Chen, Q., Zhu, L., Wang, H., 2022c. Data-driven modeling of wind waves in upper Delaware Bay with living shorelines. Ocean Eng. 257, 111669 https://doi.org/ 10.1016/j.oceaneng.2022.111669.
- Wei, Z., 2021. Forecasting wind waves in the US Atlantic Coast using an artificial neural network model: towards an AI-based storm forecast system. Ocean Eng. 237, 109646
- Xu, G., Ji, C., Xu, Y., Yu, E., Cao, Z., Wu, Q., Lin, P., Wang, J., 2023. Machine learning in coastal bridge hydrodynamics: a state-of-the-art review. Appl. Ocean Res. 134, 103511.
- Yao, J., Wu, W., 2022. Wave height forecast method with multi-step training set extension LSTM neural network. Ocean Eng. 263, 112432.
- Zhang, S., Yang, Z., Zhang, Y., Zhao, S., Wu, J., Wang, C., Wang, Y.-G., Jeng, D.-S., Nielsen, P., Li, G., 2023. Improved prediction of local significant wave height by considering the memory of past winds. Water Resour. Res. 59, e2023WR034974.
- Zhao, L., Li, Z., Qu, L., Zhang, J., Teng, B., 2023. A hybrid VMD-LSTM/GRU model to predict non-stationary and irregular waves on the east coast of China. Ocean Eng. 276, 114136.

- Zheng, Z., Ma, X., Ma, Y., Dong, G., 2020. Wave estimation within a port using a fully nonlinear Boussinesq wave model and artificial neural networks. Ocean Eng. 216, 108073.
- Zhu, L., Chen, Q., 2017. Effects of triad interactions on wave attenuation by vegetation. J. Eng. Mech. 143, 4017100.
- Zhu, L., Chen, Q., Wang, H., Capurso, W., Niemoczynski, L., Hu, K., Snedden, G., 2020. Field observations of wind waves in upper Delaware Bay with living shorelines. Estuar. Coasts 43, 739–755.